



HAL
open science

A coupled-channels model describing the low-lying 2Δ , $2 \Sigma +$ and 2Π electronic states of nickel monohydride with experimental accuracy

I. Havalyova, I. Bozhinova, A. Pashov, Amanda J. Ross, Patrick Crozet

► To cite this version:

I. Havalyova, I. Bozhinova, A. Pashov, Amanda J. Ross, Patrick Crozet. A coupled-channels model describing the low-lying 2Δ , $2 \Sigma +$ and 2Π electronic states of nickel monohydride with experimental accuracy. *Journal of Quantitative Spectroscopy and Radiative Transfer*, 2021, 272, pp.107800. 10.1016/j.jqsrt.2021.107800 . hal-03299503

HAL Id: hal-03299503

<https://hal.science/hal-03299503>

Submitted on 26 Jul 2021

HAL is a multi-disciplinary open access archive for the deposit and dissemination of scientific research documents, whether they are published or not. The documents may come from teaching and research institutions in France or abroad, or from public or private research centers.

L'archive ouverte pluridisciplinaire **HAL**, est destinée au dépôt et à la diffusion de documents scientifiques de niveau recherche, publiés ou non, émanant des établissements d'enseignement et de recherche français ou étrangers, des laboratoires publics ou privés.

A coupled–channels model describing the low-lying ${}^2\Delta$, ${}^2\Sigma^+$ and ${}^2\Pi$ electronic states of nickel monohydride with experimental accuracy

I. Havalýova, I. Bozhinova, and A. Pashov*
*Faculty of Physics, Sofia University,
5 James Bourchier Boulevard, 1164 Sofia, Bulgaria*

A. J. Ross and P. Crozet
*University of Lyon, Université Claude Bernard Lyon 1 & CNRS,
Institute Lumière Matière UMR 5309,
F-69622, Villeurbanne, France*

(Dated: July 15, 2021)

A detailed study of the three interacting low-lying electronic states ${}^2\Delta$, ${}^2\Sigma^+$ and ${}^2\Pi$ of NiH –the so called “supermultiplet” – is presented. A coupled-channels model reproduces the experimental term values of ${}^{58}\text{NiH}$, ${}^{60}\text{NiH}$ and ${}^{62}\text{NiH}$ with accuracy very close to the estimated uncertainty of 0.01 cm^{-1} . The model is based on a set of Hund’s case (a) potential curves and R -dependent coupling functions. In addition to the expected spin-orbit and various rotational couplings between the zero-order states, second-order effects are found to be important. The spin-orbit interaction is large compared to the separations between these electronic states, so that most of the observed rovibrational levels are strong mixtures of the Ω components of the multiplet. The fitting procedure proved difficult because there were no perturbation-free data to determine the starting values for the model functions. For the potential curves we were guided by previous effective Hamiltonian models; *ab initio* predictions supplied starting values for the spin-orbit and the rotational coupling functions. We believe that this model may be reliably extrapolated to higher rotational levels, with potential applications in the simulation of high temperature spectra, for example in the context of stellar atmospheres.

I. INTRODUCTION

We propose a quantum-mechanical coupled-channels model to describe the three lowest electronic states of NiH with potential energy curves, R -dependent coupling functions and Born-Oppenheimer breakdown terms. It is well-established that the rovibrational levels of the close-lying ${}^2\Delta_{5/2, 3/2}$, ${}^2\Sigma^+$ and ${}^2\Pi_{3/2, 1/2}$ states are so strongly mixed through spin-orbit coupling (References [1–5]) that rovibrational energies cannot be reproduced by single state expressions. These studies [1, 5] already found that whilst the unpaired electron on the Ni centre is mainly responsible for this spin-orbit coupling, simple Ni^+ ($3d^9$) atomic parameters cannot successfully reproduce observed spin-orbit or L-uncoupling effects. The model represents term values covered by all available experimental data [4, 6–9] supplemented by new data from resolved fluorescence experiments which located rotational levels in $v=1$ of the ${}^2\Pi_{1/2}$ and $v=2$ of the ${}^2\Sigma^+$ states for ${}^{58}\text{NiH}$ and ${}^{60}\text{NiH}$. These term values complete gaps in the energy-level distribution up to 6500 cm^{-1} above the lowest rovibrational level of the ${}^2\Delta_{5/2}$ state (see Figure 1) and were crucial in our direct potential fit.

One advantage of using radial functions rather than spectroscopic constants to generate molecular energy levels is that (assuming the use of plausible functional forms) reliable extrapolations can be made beyond the regions covered by the data. This is invaluable in predicting spectral features of high-temperature spectra. Absorption bands of metal-containing diatomics, including MH species, are seen in “cool” stellar environments, with $T \approx 3000\text{ K}$. Although laboratory work can provide direct measurements for only some parts of stellar spectra, analysis and reasoned extrapolation can produce useful compilations of molecular line lists; MoLList [10] and ExoMol [11], for example, include several monohydride entries. The ExoMol team [12] has addressed several complex spectroscopic problems, optimising *ab initio* potential curves and coupling functions to reproduce spectral data for multiple electronic states of metal oxides to produce linelists; MgO [13] and TiO [14] give just two examples of their recent work on spin-orbit coupled states. NiH, with its three low-lying doublet states (correlating with $\text{Ni}^+(3d^9\text{ }{}^2D)$ and H^- at equilibrium internuclear distance), well-removed in energy from higher-lying doublet and quartet states, provides an interesting

* pashov@phys.uni-sofia.bg

test case. It introduces complications due to strong spin-orbit interaction, sparse observations associated with widely-spaced vibrational and rotational levels, and to contributions from Born-Oppenheimer breakdown effects. Within the presented model we can reproduce observed energy levels up to about 7800 cm^{-1} above the lowest rovibronic level ($v'' = 0, J'' = 2.5$ in $X_1 \ ^2\Delta_{5/2}$) with a standard deviation of 0.014 cm^{-1} , very close to the estimated experimental uncertainty. This represents a significant improvement over the accuracy achieved by the most recent models [5] on these electronic states.

Direct fitting of diatomic molecular energy levels to vibration-rotation eigenvalues determined directly from internuclear potential energy functions is a well-established practice, offering quantum-mechanical consistency and experimental accuracy. Starting with the pioneering works by Kozman, Hinze [15] and Vidal [16], it has been particularly successful on isolated singlet states. Coxon and Hajigeorgiou [17, 18] introduced the use of analytical potential forms in their study of Born-Oppenheimer breakdown on H/D substitution in hydrogen halides.

Four low-lying $^2\Sigma^+$ states (including the double-minimum B/B' state) of CaH and CaD, formed as attractive ionic potentials cross diabatic repulsive states, were amongst the first MH diatomics to be described by a coupled-channel fit to empirical potentials [19]. Most vibrational energies in CaH and CaD were reproduced to within 5 cm^{-1} in that work. The model was refined in 2002 [20], and recent observations of excited vibrational levels in the double minimum state [21] have confirmed its validity and predictive powers.

As computational resources improved, coupled-channel models have been increasingly successful in matching experimental accuracy for rovibronic term values in pairs of interacting states, for example $^1\Sigma \sim ^1\Pi$ mixing in excited states of the alkali or alkaline earth dimers [22–25], and in representing energy levels of spin-orbit coupled states. Alkali-metal diatomics have been extensively studied in this context, because experimental work has been able to determine thousands of rovibronic level energies in many instances, showing numerous avoided crossings between states. A few (far from exhaustive) examples of such work include the deperturbation of the A/b complex associated with increasingly strong spin-orbit coupling from nP alkali atom asymptotes, in NaK [26], KRb [27] Rb₂ [28], and Cs₂ [29]. Spin-orbit interactions can achieve 50-50 mixing between states in these, making the usual v, S, Λ and Σ quantum numbers meaningless. When higher-lying electronic states are considered [21, 24, 30, 31], new difficulties arise as dominant state configurations change, and coupling functions can vary quickly with internuclear distance. In this situation cubic-spline pointwise representation (as in [22, 24, 30, 31]) may become more convenient than analytical functional forms. This was found to be the case for the coupled states problem in NiH, discussed in the following pages.

In extending the coupled-potentials approach to represent the $^2\Delta_{5/2, 3/2}, ^2\Sigma^+$ and $^2\Pi_{3/2, 1/2}$ states of NiH, we face the complication of parameter correlation between strongly interacting channels. In such a situation, theoretical predictions for the potential energy curves and the coupling functions become especially valuable. Open-shell diatomic systems in general are a challenge for theoretical work, as discussed in Ref. [12] for example; the particular problems associated with 3d metal hydrides MH, and notably with their excited electronic states, are also described in the literature, for example in Refs. [32–34]. *Ab initio* studies of nickel hydride, e.g. [35], give a much broader view of the electronic structure of NiH than experiment has yet been able to generate. Marian's multi-reference double-excitation CI calculations [2, 3] are particularly pertinent, as they give spin-orbit coupling functions that by construction include contributions from electronic configurations other than $\text{Ni}^+ (3d^9 \ ^2D)$. They provided a criterion for 'well-behaved' R -dependent functions throughout this work, and imposed asymptotic behaviour.

In the next section, II, we give an overview of the data available, giving details only for previously unreported transitions. The Hamiltonian used to model the experimental energy levels of the ground state supermultiplet is discussed in detail in section III. The fitting procedure and its outcome are summarised in sections IV and V respectively. Discussions and conclusions are presented in section VI.

II. TERM ENERGIES: INPUT DATA FOR THE COUPLED-STATES MODEL

The rovibrational term energy data for the three lowest-lying electronic states of NiH extend 7800 cm^{-1} above the first rovibrational level of the electronic ground state. Most data come from electronic transitions, recorded as laser-induced fluorescence in Lyon [4, 6], but some far- and mid-infrared transitions seen in laser resonance in the 1990's [7, 8], and pure rotational transitions, measured by microwave spectroscopy [9], give a sharper definition of the lowest levels of the $^2\Delta$ state.

Resolved laser-induced fluorescence experiments had pumped excited $^2\Phi_{7/2}, ^2\Delta_{5/2}, ^2\Pi_{3/2}$ electronic states from $v=0$ in the electronic ground state ($X_1 \ ^2\Delta_{5/2}$), giving strong fluorescence for $\Delta\Lambda = \Delta\Omega$ transitions, and weaker signals for $\Delta\Lambda = \Delta\Omega \pm 1$. But spectra were much richer than expected, because collisional energy transfer in NiH was found to be unusually successful in populating numerous rotational levels of close-lying excited electronic states without strict selection rules. $\Omega' = 1/2$ states are populated only through collisions (being electric-dipole forbidden from the $^2\Delta_{5/2}$ ground state), and many of the $\Omega' = 3/2$ states are more effectively populated through collisions than

by direct excitation.

Since all information on the ${}^2\Pi_{1/2}$ and ${}^2\Sigma^+$ states comes exclusively through fluorescence from $\Omega' = 1/2$ and $3/2$ states that are better populated through collisions than via direct laser excitation, we re-recorded Fourier-transform resolved fluorescence spectra (nominal resolution 0.05 cm^{-1}) following excitation via strong transitions (Q(2.5) 1-0 B-X₁ and R(2.5) 0-0 F-X₁), in ${}^{58}\text{NiH}$ and ${}^{60}\text{NiH}$. We averaged up to 200 scans for ${}^{60}\text{NiH}$ to reduce baseline noise. NiH was formed in a dc sputter source (described in detail in ref. [36]), with a 10 % H₂/Ar gas mixture flowing through a drilled solid nickel cathode (natural abundances ${}^{58}\text{Ni}$ 68.1%, ${}^{60}\text{Ni}$ 26.2%; ${}^{61}\text{Ni}$ 1.1%, ${}^{62}\text{Ni}$ 3.6%, ${}^{64}\text{Ni}$ 0.9%), then through a copper loop anode. The current was typically 250 mA, and the pressure around 1 Torr. The discharge plasma was probed about 1 cm beyond the electrodes with output from a tuneable single mode cw dye laser (typical power 300 mW using rhodamine 6G dye), producing bright-by-eye orange fluorescence. Backwards fluorescence was focused on to the entrance aperture of the Fourier transform spectrometer using a flat pierced mirror and a pair of focusing lenses to respect the f/4 aperture of the instrument. Rotationally relaxed bands could be followed to higher J than before. Of particular interest were transitions from an $\Omega' = 0.5$ state lying 16650 cm^{-1} above the ground state (first identified in NiD[5], now observed for the first time in NiH), as they finally located f -parity levels of $v=1$, ${}^2\Pi_{1/2}$ in ${}^{58}\text{NiH}$. The ${}^{58}\text{NiH}$ wavenumbers are listed in Table 1. Equally important for the subsequent fits were some lines around 11600 cm^{-1} assigned as the 0-2 band of the I[$\Omega' = 3/2$] - ${}^2\Sigma^+$ system. These gave the first observation of $v=2$ in the ${}^2\Sigma^+$ state.

Wherever possible, lower-state energy levels have now been determined from transitions measured in the new spectra, because we found significant shifts (sometimes as large as 0.02 cm^{-1}) between current wavenumbers and those derived from ‘direct’ fluorescence, notably from the $\Omega' = 3/2$ states in older spectra from Lyon. Well-resolved peaks in the Fourier transform spectra are usually determined to one-tenth of the full-width-at-half-maximum linewidth, which in this case should have been 0.005 cm^{-1} . Measured line positions are usually reproducible within this limit, but emission spectra are susceptible to show systematic frequency-dependent drifts in absolute line positions, if light is injected slightly off the instrumental optical axis. This problem becomes more obvious if the spectrum covers a wide wavenumber range, in this instance 7000 cm^{-1} . In this particular instance, the calibration discrepancy could arise from a real difference in the reference wavelength of the instrument, as the single-mode HeNe laser calibrating the spectrometer had been changed in the interim. The wavenumber scales of the recent spectra are considered to be the more reliable because they have been validated against argon lines [37], produced when sputtering nickel in an Ar/H₂ mixture to form NiH.

The level energies for ${}^{58,60,62}\text{NiH}$ were determined from separate term-value fits. The term energies are referenced to the lowest rotational level of each isotopologue, ($\text{T}[X_1\ {}^2\Delta_{5/2}, v=0, J=2.5, e \text{ and } f] = 0.0\text{ cm}^{-1}$). The spread of observed energy terms in the low-lying states of ${}^{58}\text{NiH}$ is illustrated in Fig. 1. Markers indicate predictions for the still-unobserved vibrational states ${}^2\Pi_{1/2} v=2$ and ${}^2\Pi_{3/2} v=3$ above 6500 cm^{-1} . Fig. 1 represents 358 energy terms for ${}^{58}\text{NiH}$ determined from 2862 spectral lines. There is less information on the low- Ω'' states for the minor isotopologues. We have 275 terms for ${}^{60}\text{NiH}$ (determined from 834 spectral lines) and 120 terms for ${}^{62}\text{NiH}$ (determined from 348 spectral lines). All transition wavenumbers and the corresponding term values are provided as a supplementary material. Lower state term energies (input for the coupled channels fit) were uniformly assigned an uncertainty of 0.01 cm^{-1} .

III. THE HAMILTONIAN, COUPLING OPERATORS AND THEIR MATRIX ELEMENTS

The model Hamiltonian used here is based on the ‘supermultiplet’ analysis of the ${}^2\Delta \sim {}^2\Sigma^+ \sim {}^2\Pi$ interacting states of nickel monohydride reported by Gray *et al.* in Ref. [1] about 30 years ago. The implication of the supermultiplet treatment for NiH is that the formation of a covalent bond between H and Ni involves the H(1s) and Ni(4s) electrons, and that the remaining valence electrons are essentially non-bonding electrons located on the nickel ion. The ground state Ni⁺ ion has a $3d^9$ configuration [37]. The model assumes that the magnitude of spin-orbit interactions and \mathbf{L}_\pm matrix elements in the associated molecular states match atomic parameters for $3d^9$ Ni⁺ ion 2D , with $L = 2$, $S = 1/2$ and $\zeta = 602.78\text{ cm}^{-1}$.

A. Model Hamiltonian

The total Hamiltonian of the system ${}^2\Delta \sim {}^2\Sigma^+ \sim {}^2\Pi$ can be written as:

$$\mathbf{H} = \mathbf{T}_e(r) + \mathbf{T}_N(R) + \mathbf{H}_{\text{rot}}(R, \theta, \varphi) + \mathbf{V}(R, r) + \mathbf{H}_{\text{SO}} + \mathbf{H}_{\text{sr}} .$$

Here $\mathbf{T}_e(r)$ is the kinetic energy operator of the electrons, $\mathbf{T}_N(R)$ and $\mathbf{H}_{\text{rot}}(R, \theta, \varphi)$ are the vibrational and rotational

TABLE I. Observed transitions (in cm^{-1}) from the $[16.6]0.5$ state in ^{58}NiH . Data for ^{60}NiH can be found in the supplementary materials [38]

$[16.6]0.5 - {}^2\Sigma^+ v''=0$ J''	R_e	R_f	P_e	P_f	Q_{ef}	Q_{fe}
0.5	14687.157					
1.5	14739.755			14522.195	14607.396	14599.306
2.5	14792.702			14466.738	14607.181	14596.650
3.5	14842.406			14411.789	14607.841	14594.206
4.5	14890.095			14357.794	14605.993	14592.175
5.5	14936.416			14305.184	14603.076	14590.668
6.5	14981.224			14254.169	14599.936	14589.644
7.5	15025.095			14205.040	14596.630	14588.869
8.5				14157.722		14587.826
9.5				14112.067		
10.5				14067.790		
11.5				14024.525		
$[16.6]0.5 - {}^2\Sigma^+ v''=1$ J''	R_e	R_f	P_e	P_f	Q_{ef}	Q_{fe}
0.5	12888.094					
1.5	12940.121			12727.011	12812.204	12799.677
2.5	12992.835			12673.624	12814.073	12796.778
3.5	13042.564			12621.138	12817.188	12794.364
4.5	13090.509			12569.998	12818.204	12792.583
5.5	13137.127			12520.619	12818.538	12791.375
6.5				12473.290	12819.039	
7.5				12428.171		
8.5				12385.248		
9.5				12344.338		
10.5				12305.155		
$[16.6]0.5 - {}^2\Pi_{1/2} v''=0$ J''	R_e	R_f	P_e	P_f	Q_{ef}	Q_{fe}
0.5	13262.670	13200.349				
1.5	13283.984	13203.962				
2.5	13305.464	13207.561		13162.849		
3.5	13323.633	13211.412		13136.294		
4.5	13339.893	13215.696		13109.758		
5.5	13355.068	13220.449	13151.580	13083.522		
6.5	13369.293	13225.609	13138.662	13057.803		
7.5		13230.911	13125.125	13032.667		
8.5		13236.004	13111.360	13008.039		
9.5		13240.530		12983.708		
10.5		13244.071		12959.351		
$[16.6]0.5 - {}^2\Pi_{1/2} v''=1$ J''	R_e	R_f	P_e	P_f	Q_{ef}	Q_{fe}
0.5	11463.522	11398.875				
1.5	11486.832	11402.082		11387.195		
2.5	11510.912	11405.763	11385.185	11361.036		
3.5	11532.371	11410.129	11379.891	11335.013		
4.5	11552.726	11415.397	11375.728	11309.452		
5.5	11572.975	11421.574	11369.486	11284.634		
6.5	11593.502	11428.560	11362.902	11260.753		
7.5	11615.185	11436.113		11237.866		
8.5		11443.886		11215.915		
9.5		11451.485		11194.656		
10.5				11173.772		
11.5				11152.908		
$[16.6]0.5 - {}^2\Pi_{3/2} v''=0$ J''	R_e	R_f	P_e	P_f	Q_{ef}	Q_{fe}
0.5						
1.5	14185.299	14059.540			14129.862	14044.847
2.5	14216.982	14050.312	14091.251	14005.599	14146.035	14020.932
3.5	14244.935	14040.699	14092.482	13965.588	14161.621	13996.752
4.5	14270.549	14030.814	14093.562		14173.067	13972.631
5.5	14294.602	14020.665			14181.656	13948.852
6.5		14010.140				13925.533
7.5		13998.962				13902.623
8.5		13986.789				
9.5		13973.249				13857.361
10.5		13857.985				13834.384
11.5						13810.756

part of the total nuclear kinetic energy operator. $\mathbf{V}(R, r)$ is the potential energy. \mathbf{H}_{SO} and \mathbf{H}_{sr} represent the relativistic spin-orbit and spin-rotation Hamiltonians.

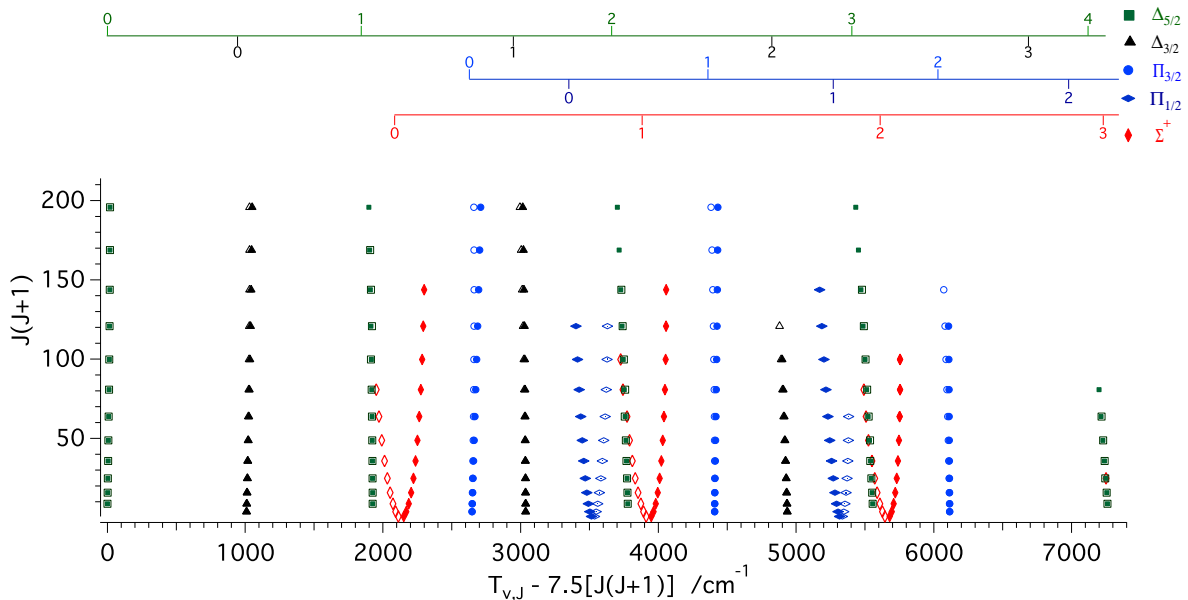


FIG. 1. Plot of rotationally-reduced energy terms ($T_{v,J} - 7.5J(J+1) \text{ cm}^{-1}$) in ^{58}NiH (relative to $T = 0.0 \text{ cm}^{-1}$ for $J=2.5$, $v=0$ in $^2\Delta_{5/2}$), with vibrational assignments. Open symbols indicate e parity labels, solid ones f . Levels $v=2$ in $^2\Pi_{1/2}$ and $v=3$ in $^2\Pi_{3/2}$ above 6500 cm^{-1} remain unobserved.

We will treat the coupled channels problem with Hund's case (a) basis set functions which are labeled with the quantum numbers associated with the electronic-spin-rotational part of the full molecular wavefunction. Symmetrized representations of the basis states are then applied [39], with well-defined e/f symmetry, taking the following general form (excluding Σ^- states):

$$|\Lambda\Sigma\Sigma J\Omega M; e/f\rangle = 2^{-1/2} [|\Lambda\Sigma\Sigma J\Omega M\rangle \pm |-\Lambda S - \Sigma J - \Omega M\rangle] . \quad (1)$$

In this representation there are five electronic-spin-rotation basis functions, corresponding to the Hund's case(a) electronic states $^2\Delta_{5/2}$, $^2\Delta_{3/2}$, $^2\Sigma_{1/2}^+$, $^2\Pi_{1/2}$ and $^2\Pi_{3/2}$. The total wavefunction can then be written as a superposition of these basis functions (denoted for simplicity as $|i\rangle$):

$$\Psi(R, r) = \sum_{i=1}^5 \phi_i(R) |i\rangle ,$$

where $\phi_i(R)$ are R -dependent mixing coefficients corresponding to solutions of the set of coupled equations:

$$\sum_{j=1}^5 H_{ij} \phi_j(R) = E \phi_i(R) ,$$

where H_{ij} are the R -dependent matrix elements of the total Hamiltonian $\langle i | \mathbf{H} | j \rangle$, calculated between the basis functions.

Each term of the total Hamiltonian will be considered separately and its matrix elements will be evaluated in terms of the basis set functions. The interactions involving the orbital angular momentum \mathbf{L} should be considered as specific to this case, because \mathbf{L}^2 is not usually a well-defined quantity in a diatomic molecule, where spherical symmetry is broken. By accepting L as an approximately good quantum number for these states of NiH [1], with $L = 2$ due to the ^2D ground state of the Ni^+ , we will assume that the basis functions (1) are approximate eigenstates of \mathbf{L}^2 . Corrections to this assumption will be introduced by multiplying its eigenvalue by an R -dependent function. The more valid the assumption, the closer the function will be to unity.

The basis functions are chosen to be eigenfunctions of the electronic Hamiltonian and its diagonal elements $\langle i | \mathbf{T}_e(r) + \mathbf{V}(R, r) | i \rangle = U_i(R)$ are the electronic potential energy curves.

B. Electronic-spin-rotational couplings

The term \mathbf{H}_{rot} has both diagonal and off-diagonal matrix elements [39]:

$$\mathbf{H}_{\text{rot}} = \frac{1}{2\mu R^2} \left[(\mathbf{J}^2 - \mathbf{J}_z^2) + (\mathbf{L}^2 - \mathbf{L}_z^2) + (\mathbf{S}^2 - \mathbf{S}_z^2) \right. \quad (2a)$$

$$\left. - (\mathbf{J}_+\mathbf{S}_- + \mathbf{J}_-\mathbf{S}_+) - (\mathbf{J}_+\mathbf{L}_- + \mathbf{J}_-\mathbf{L}_+) + (\mathbf{L}_+\mathbf{S}_- + \mathbf{L}_-\mathbf{S}_+) \right] \quad (2b)$$

where the operators \mathbf{J} , \mathbf{J}_+ and \mathbf{J}_- satisfy the anomalous commutation relations ([40]) in the rotating molecular frame. The first three terms (2a) constitute the diagonal part of the rotational Hamiltonian with matrix elements equal to $(\hbar^2/2\mu R^2)[J(J+1) - \Omega^2 - \Lambda^2 + S(S+1) - \Sigma^2]$. The contribution of the mean value of the electronic angular momentum \mathbf{L}^2 will be treated as a correction to the potential energy curve.

The terms with non-zero off-diagonal matrix elements (2b) connect states or their multiplet components differing by the values of two of the projection quantum numbers Λ , Σ or Ω .

a. Spin-uncoupling The Spin-uncoupling operator

$$\mathbf{H}_{\text{JS}} = -\frac{1}{2\mu R^2} (\mathbf{J}_+\mathbf{S}_- + \mathbf{J}_-\mathbf{S}_+)$$

mixes the two Ω -components of the ${}^2\Pi$ and ${}^2\Delta$ electronic states.

$$\begin{aligned} \langle {}^2\Pi_{3/2} | \mathbf{H}_{\text{JS}} | {}^2\Pi_{1/2} \rangle &= -B \sqrt{J(J+1) - \Omega\Omega'} \sqrt{S(S+1) - \Sigma\Sigma'} \\ &= -B \sqrt{Y^2 - 1} \end{aligned} \quad (3)$$

where Ω , Ω' , Σ and Σ' are the corresponding quantum numbers of the states involved, $Y = J+1/2$ and $B = \hbar^2/(2\mu R^2)$. Similarly for the ${}^2\Delta$ states :

$$\langle {}^2\Delta_{5/2} | \mathbf{H}_{\text{JS}} | {}^2\Delta_{3/2} \rangle = -B \sqrt{Y^2 - 4} \quad (4)$$

With B of the order of the rotational constant $B_e \approx 7.5 \text{ cm}^{-1}$, the spin-uncoupling matrix element exceeds 100 cm^{-1} for the highest observed rotational levels ($J = 15.5$).

The e - and f -symmetry components of an isolated ${}^2\Sigma^+$ state in the symmetrized representation of case (a) are always non-degenerate, due to the spin-uncoupling operator. Its matrix element is:

$$\langle {}^2\Sigma^+; e/f | \mathbf{H}_{\text{JS}} | {}^2\Sigma^+; e/f \rangle = \mp BY \quad (5)$$

where the sign $-/+$ corresponds to e/f -symmetry levels respectively. Parity selection rules forbid mixing between different symmetry levels. In contrast, the e and f levels of isolated ${}^2\Pi$ or ${}^2\Delta$ states would be degenerate.

b. L-uncoupling The L-uncoupling operator

$$\mathbf{H}_{\text{JL}} = -\frac{1}{2\mu R^2} (\mathbf{J}_+\mathbf{L}_- + \mathbf{J}_-\mathbf{L}_+)$$

connects states with $\Delta\Lambda = \Delta\Omega = \pm 1$. Its non-vanishing matrix elements are:

$$\begin{aligned} \langle {}^2\Delta_{3/2} | \mathbf{H}_{\text{JL}} | {}^2\Pi_{1/2} \rangle &= -B \sqrt{J(J+1) - \Omega\Omega'} \sqrt{L(L+1) - \Lambda\Lambda'} \beta_{\Pi\Delta}(R) \\ &= -2B \beta_{\Pi\Delta}(R) \sqrt{Y^2 - 1} \end{aligned} \quad (6)$$

$$\langle {}^2\Delta_{5/2} | \mathbf{H}_{\text{JL}} | {}^2\Pi_{3/2} \rangle = -2B \beta_{\Pi\Delta}(R) \sqrt{Y^2 - 4} \quad (7)$$

$$\langle {}^2\Pi_{3/2} | \mathbf{H}_{\text{JL}} | {}^2\Sigma^+ \rangle = -\sqrt{6} B \beta_{\Pi\Sigma}(R) \sqrt{Y^2 - 1} \quad (8)$$

The $\beta_{\Lambda\Lambda'}$ functions take into account the possible R -dependence of the matrix element including the \mathbf{L}_+ operator between electronic states Λ and Λ' . If the assumption that L is a good quantum number is strictly valid, $\beta_{\Lambda\Lambda'}$ should be exactly equal to 1 and we began by imposing this constraint, following Gray *et al* [1]. $\beta_{\Lambda\Lambda'}$ functions were introduced as the fit progressed, when it became clear that the experimental data require small deviations from the $L=2$ approximation.

In the particular case of interacting ${}^2\Sigma^+$ and ${}^2\Pi_{1/2}$ states, a special manifestation of the L-uncoupling operator results in non-zero matrix element because of interference effects between $\Delta\Omega = +1$ and $\Delta\Omega = -1$ basis states in the transformation from unsymmetrized to symmetrized basis set. This gives rise to a symmetry-dependent contribution:

$$\langle {}^2\Pi_{1/2}; e/f | \mathbf{H}_{\text{JL}} | {}^2\Sigma^+; e/f \rangle = \mp \sqrt{6} B \beta_{\Pi\Sigma}(R) \sqrt{Y^2 + 1} \quad (9)$$

where the $-/+$ sign again corresponds to e/f levels.

c. Spin-electronic coupling In the context of our ${}^2\Delta - {}^2\Sigma^+ - {}^2\Pi$ system, the spin-electronic operator

$$\mathbf{H}_{\text{LS}} = \frac{1}{2\mu R^2} (\mathbf{L}_+ \mathbf{S}_- + \mathbf{L}_- \mathbf{S}_+)$$

ouples the same fine-structure components as the spin-orbit operator ($\Delta\Omega = 0$):

$$\begin{aligned} \langle {}^2\Delta_{3/2} | \mathbf{H}_{\text{LS}} | {}^2\Pi_{3/2} \rangle &= -B \sqrt{S(S+1) - \Sigma\Sigma'} \sqrt{L(L+1) - \Lambda\Lambda'} \beta_{\Pi\Delta}(R) \\ &= 2B \beta_{\Pi\Delta}(R) \end{aligned} \quad (10)$$

$$\langle {}^2\Pi_{1/2} | \mathbf{H}_{\text{LS}} | {}^2\Sigma^+ \rangle = \sqrt{6} B \beta_{\Pi\Sigma}(R). \quad (11)$$

where $\beta_{\Pi\Delta}$ and $\beta_{\Pi\Sigma}$ are the same β functions as in Eqs. (6)-(7) and Eqs. (8)-(9) respectively.

C. Spin-orbit coupling

The spin-orbit operator introduces both diagonal and off-diagonal matrix elements. Diagonal spin-orbit coupling exists within the Ω -components of the ${}^2\Pi$ state (${}^2\Pi_{1/2}$, ${}^2\Pi_{3/2}$) and the ${}^2\Delta$ state (${}^2\Delta_{3/2}$, ${}^2\Delta_{5/2}$). Its matrix elements can be written as [39]:

$$\langle {}^2\Pi_{\Omega} | \mathbf{H}_{\text{SO}} | {}^2\Pi_{\Omega} \rangle = \pm \frac{A_{\Pi\Pi}(R)}{2} \quad (12)$$

$$\langle {}^2\Delta_{\Omega} | \mathbf{H}_{\text{SO}} | {}^2\Delta_{\Omega} \rangle = \pm A_{\Delta\Delta}(R) \quad (13)$$

where the plus sign corresponds to the matrix elements between components with positive Σ values. $A_{\Pi\Pi}(R)$ and $A_{\Delta\Delta}(R)$ represent the diagonal spin-orbit splitting functions for ${}^2\Pi$ and ${}^2\Delta$ states which are to be determined. To give an order of magnitude, the spin-orbit splitting between ${}^2D_{5/2}$ and ${}^2D_{3/2}$ in $3d^9 \text{Ni}^+$ is 1506.94 cm^{-1} , giving an atomic spin-orbit parameter $\zeta = 602.78 \text{ cm}^{-1}$. The functions describing $A_{\Pi\Pi}$ and $A_{\Delta\Delta}$ for the lowest ${}^2\Pi$ and the ${}^2\Delta$ states of NiH are expected to be close to this value.

The states differing by $\Delta\Lambda = \pm 1$ and $\Delta\Sigma = \mp 1$ so that $\Delta\Omega = 0$ are coupled by an off-diagonal spin-orbit term:

$$\langle {}^2\Pi_{1/2} | \mathbf{H}_{\text{SO}} | {}^2\Sigma_{1/2}^+ \rangle = \frac{\sqrt{6}}{2} \alpha_{\Pi\Sigma}(R) \quad (14)$$

$$\langle {}^2\Delta_{3/2} | \mathbf{H}_{\text{SO}} | {}^2\Pi_{3/2} \rangle = \alpha_{\Pi\Delta}(R) \quad (15)$$

where $\alpha_{\Lambda\Lambda'}(R)$ is the spin-orbit R -dependent coupling function connecting the electronic states Λ and Λ' . Here, the factors $\sqrt{6}$ and 2 come again from the assumption that $L = 2$. The $\alpha_{\Lambda\Lambda'}(R)$ values are expected to be close to $\zeta = 602.78 \text{ cm}^{-1}$.

D. Spin-Rotation coupling

Spin-rotation is another relativistic effect to be considered but its contribution is expected to be much smaller than that of the spin-orbit interaction. The contribution of the diagonal matrix elements $\beta'(R) [\Sigma^2 - S(S+1)]$ can be effectively added to the diagonal part of the Hamiltonian. But off-diagonal spin-rotation matrix elements $\beta'(R) \sqrt{J(J+1) - \Omega(\Omega \pm 1)} \sqrt{S(S+1) \pm \Sigma(\Sigma \pm 1)}$ cannot be distinguished from the matrix elements of the spin-uncoupling operator from Eq. (3), (4) and (5): the same states interact through these two operators with identical dependence on the quantum numbers. We have therefore grouped them as $\gamma(R)$ functions:

$$\langle {}^2\Pi_{3/2} | \mathbf{H}_{\text{JS}} + \mathbf{H}_{\text{sr}} | {}^2\Pi_{1/2} \rangle = -B \gamma_{\Pi}(R) \sqrt{Y^2 - 1}$$

$$\langle {}^2\Delta_{5/2} | \mathbf{H}_{\text{JS}} + \mathbf{H}_{\text{sr}} | {}^2\Delta_{3/2} \rangle = -B \gamma_{\Delta}(R) \sqrt{Y^2 - 4}$$

$$\langle {}^2\Sigma^+; e/f | \mathbf{H}_{\text{JS}} + \mathbf{H}_{\text{sr}} | {}^2\Sigma^+; e/f \rangle = \mp B \gamma_{\Sigma}(R) Y.$$

where $\gamma(R) = 1 - \beta'(R)$. The gamma functions should be close to unity, if spin-rotation effects are small.

E. Born-Oppenheimer breakdown corrections to the Hamiltonian

It is well established that the Born-Oppenheimer approximation breaks down on isotopic substitution with simple mass-dependent corrections: at the level of the adiabatic approximation, different effective potential energy curves are predicted for each isotopologue. According to Bunker and Moss [41], the primary mass-dependent correction to the Born-Oppenheimer potential energy curve $U^{\text{BO}}(R)$ comes from a first-order correction term $\Delta U_i(R) = \langle i | \mathbf{T}_N(R) | i \rangle$. This term is usually called the adiabatic or diagonal Born-Oppenheimer correction. When data for a single isotopologue are treated, the fitted potential curves may be called adiabatic, since they include this correction, i.e. $U_i(R) = U_i^{\text{BO}}(R) + \Delta U_i(R)$. It may be necessary to account for the mass dependence of the adiabatic correction when two or more isotopologues are treated simultaneously.

In addition, there are mass-dependent second-order corrections due to $\mathbf{T}_N(R)$ and $\mathbf{H}_{\text{rot}}(R, \theta, \phi)$. The rotationally dependent correction due to $\mathbf{H}_{\text{rot}}(R, \theta, \phi)$ can be written as:

$$f_i(R) = \sum_k \frac{\langle i | \mathbf{H}_{\text{rot}}(R, \theta, \phi) | k \rangle^2}{U_i(R) - U_k(R)}.$$

Adopting the form of \mathbf{H}_{rot} presented in Section III B, and taking the summation over remote electronic states (other than those included explicitly in the model), the correction becomes:

$$f_i(R) = \left(\frac{\hbar^2}{2\mu R^2} \right)^2 \left(q_i(R)J(J+1) + g_i(R) \right).$$

The $q_i(R)$ function regroups all the R -dependent terms in $J(J+1)$. They arise from the L- and spin-uncoupling part of \mathbf{H}_{rot} . The $g_i(R)$ function comes from the summation over the contributions due to the spin-electron coupling, which are J independent. Strictly speaking, the $J(J+1)$ dependence of the correction term is valid only for a $^1\Sigma$ state affected by a distant $^1\Pi$ state through the L-uncoupling operator. When states other than $^1\Sigma$ are considered, a constant should be added to $J(J+1)$ (see the matrix elements of the L-uncoupling operator in section III B); its contribution is folded into the $g_i(R)$ function. We were not able to determine the contribution of the $g_i(R)$ function; its effects were presumably swamped in $U_i(R)$. The J -dependent $q_i(R)$ contribution was significant, giving

$$f_{i,e/f}(R) = \left(\frac{\hbar^2}{2\mu R^2} \right)^2 q_{i,e/f}(R)J(J+1),$$

accounting for possible differences between the e - and f - symmetries. This form for the J -dependent Born-Oppenheimer breakdown (BOB) correction differs from that used by Le Roy in [42], treating Born-Oppenheimer breakdown in HF/DF (i.e. a case with only one isotope of the heavy atom). The apparent difference is in the mass dependence. Here we have $1/\mu^2$, whereas according to [42], there are two corrections with mass dependence $1/(\mu M_{\text{H}})$ and $1/(\mu M_{\text{Ni}})$. Due to the much lighter hydrogen, the main contribution is expected to come from the term with $1/(\mu M_{\text{H}})$ and its mass dependence is very close to $1/\mu^2$, because $\mu \approx M_{\text{H}}$.

The rotational corrections $f_i(R)$, change the R -dependence of the centrifugal potential as J increases. The $f_i(R)$ corrections can be different for e and f symmetry levels; this would be the case of a $^1\Pi$ state showing Λ -doubling through the influence of a remote $^1\Sigma^+$ state.

The Hamiltonian matrix for the present problem is shown schematically in Fig. 2, indicating the operators whose explicit forms have been detailed in the text above. H_{ii} denotes the sum of the diagonal Hund's case (a) operators $T_N(R) + U_i(R) + H_{\text{rot}}(R) + f_i(R)$.

The various functions needed to model the experimental data are determined through non-linear least squares fits. They are: three potential energy curves (PECs), two diagonal $A(R)$ and two off-diagonal $\alpha(R)$ functions for the spin-orbit interaction, the $\beta(R)$ and $\gamma(R)$ functions associated with the rotational interactions, the $q_{e/f}(R)$ second-order correction functions.

IV. COMPUTATIONS, DEPERTURBATION PROCEDURE AND FITTING OF THE DATA

The fitting procedure was initiated on the measured data for ^{58}NiH , for which we have the widest distribution of vibrational and rotational quantum numbers among the set of electronic term values. The ^{60}NiH and ^{62}NiH data

FIG. 2. Hamiltonian matrix for the present problem. Symbols of the relevant coupling operators are indicated; the explicit form of the matrix elements are explained in the text. $H_{ii} = T_N(R) + U_i(R) + H_{\text{rot}}(R) + f_i(R)$.

$$\begin{array}{ccccc}
 & {}^2\Sigma_{1/2}^+ & {}^2\Pi_{1/2} & {}^2\Pi_{3/2} & {}^2\Delta_{3/2} & {}^2\Delta_{5/2} \\
 \left(\begin{array}{ccccc}
 H_{11} + H_{11,ef}^{\text{JS}} & H_{12}^{\text{SO}} + H_{\Sigma\Pi,ef}^{\text{LJ}} + H_{\Sigma\Pi}^{\text{LS}} & H_{\Sigma\Pi}^{\text{LJ}} & 0 & 0 \\
 \text{symm} & H_{22} + H_{\text{III}}^{\text{SO}} & H_{23}^{\text{JS}} & H_{\Delta\Pi}^{\text{LJ}} & 0 \\
 \text{symm} & \text{symm} & H_{33} + H_{\text{III}}^{\text{SO}} & H_{34}^{\text{SO}} + H_{\Pi\Delta}^{\text{LS}} & H_{\Pi\Delta}^{\text{LJ}} \\
 0 & \text{symm} & \text{symm} & H_{44} + H_{\Delta\Delta}^{\text{SO}} & H_{45}^{\text{JS}} \\
 0 & 0 & \text{symm} & \text{symm} & H_{55} + H_{\Delta\Delta}^{\text{SO}}
 \end{array} \right) \begin{array}{l}
 {}^2\Sigma_{1/2}^+ \\
 {}^2\Pi_{1/2} \\
 {}^2\Pi_{3/2} \\
 {}^2\Delta_{3/2} \\
 {}^2\Delta_{5/2}
 \end{array}
 \end{array}$$

(natural abundances 26% and 4%) represent a subset of this distribution. They were used as a control as the fit of ^{58}NiH progressed; we monitored ^{60}NiH and ^{62}NiH energies computed from the optimized potentials and coupling curves for ^{58}NiH using appropriate reduced masses to be sure that the ‘‘obs-calc’’ differences are not unreasonable. In the final stage of the fitting process, experimental data from all three isotopologues were treated simultaneously.

The calculated energies are obtained as eigenvalues of the Hamiltonian (Fig. 2) discussed in the previous section. The numerical solution of the system of five coupled Schrödinger equations (III A) is based on the Fourier Grid Hamiltonian method, developed as a computational method for time-dependent quantum-mechanical problems [43] and for the calculation of bound states of time-independent problems [44] and extensively applied in molecular spectroscopy. An equidistant grid with $N_{\text{grid}} = 170$ points for internuclear distances $0.75 \text{ \AA} - 3.0 \text{ \AA}$ covers the available range of experimental observations with the required accuracy.

In a matrix representation, the computed Hamiltonian has dimensions $5N_{\text{grid}} \times 5N_{\text{grid}}$ over the discretized R values. A set of calculated energies and their corresponding eigenvectors defining the mixing coefficients $\phi_i(R)$ (from Eq.III A) are obtained after diagonalization of this matrix. The calculated energies are first referenced to the calculated energy of the level $v = 0, J = 2.5$ of the ground ${}^2\Delta_{5/2}$ state for the corresponding symmetry and isotopologue and then are introduced in a standard non-linear least-squares fitting procedure to minimize the χ^2 merit function:

$$\chi^2 = \sum_{k=1}^N \frac{(E_k^{\text{exp}} - E_k^{\text{calc}})^2}{N} \times \omega_k^2 \quad (16)$$

weighted either according to experimental uncertainty $\omega_k^2 = \sigma_k^{-2}$, or using the Robust Fit method proposed by Watson [45] to reduce the effects of outliers:

$$\omega_k^2 = \frac{1}{\sigma_k^2 + 0.3 (E_k^{\text{exp}} - E_k^{\text{calc}})^2}$$

The PECs and the matrix elements of the model Hamiltonian were defined as spline pointwise functions of the internuclear distance, where the values of the spline points are themselves the parameters to be optimized in the fit. This is a convenient option because of its simplicity. For most of the fitted functions, we have reasonable estimations for their magnitude, so we have very good starting points for the fitting routine. Moreover, during the fit serious deviations from a physically reasonable values show up easily, and may be controlled.

As a starting point for the potential energy curves we derived RKR potentials based on the available deperturbed Dunham parameters [1, 5]. Initial diagonal and off-diagonal spin-orbit parameters were fixed at their atomic values which are around 603 cm^{-1} [1]. The initial values of the rotational coupling parameters $\beta(R)$ and $\gamma(R)$ were fixed at the expected constant value of 1.0. The second order $q(R)$ parameters initially were fixed to some small value of $10^{-5} \text{ 1/cm}^{-1}$. The spin-orbit functions $\alpha_{\Lambda\Lambda'}(R)$ and $A_{\Lambda\Lambda}(R)$ were constrained to approach the atomic values at large

internuclear distances by fixing the outermost point for each of them. The remaining spin-orbit points were gradually floated during the fit. The rotational functions were similarly released, constraining their asymptotic values to unity.

The main strategy to minimize χ^2 in Eq. (16) was a nonlinear least-squares iterative fit based on the method of Singular Value Decomposition (SVD) [46] using a wrapper procedure around a standard LAPACK routine provided by SciPy module [47]. The SVD method offers a way to order the fitted parameters (or their linear combinations) according to their impact on χ^2 . So it is possible to choose and to vary only the set of most significant parameters (or their combinations), while leaving the values of the rest unchanged. This avoids having the fit return unreasonable numbers with huge standard deviations for highly correlated parameters. This approach, by reducing the effective number of free parameters, has proved already to be very efficient in single channel [48] and multichannel [24, 31] fits. All computations were performed using the recently-developed open-source Python package for coupled-channels calculations [49].

The fitting procedure began with ^{58}NiH data only. It was not straightforward, but iterated through a sequence of improvements of the model functions. Initially, when discrepancies between the calculated and experimental energies were very large, only the model functions that were expected to have major impact on the level positions and splittings were optimized, namely the three PECs $U_i(R)$, the spin-orbit $A(R)$ and $\alpha(R)$ and the rotational $\beta(R)$ coupling functions. A few transitions that led to serious outliers in the term-value data were re-assigned at this point. To improve the unweighted rms deviation beyond about 0.5 cm^{-1} the weaker interactions had to be introduced and optimized as well. A systematic trend in residuals between the e - and the f -symmetry levels was removed by adding the second-order $q_{i,e/f}(R)$ correction. Introducing the $\gamma(R)$ functions reduced the final root-mean-square (rms) deviations of the fit still further.

The analysis and fitting procedure were particularly complicated on two accounts. On the one hand, we have five channels, coupled by strong and numerous interactions, inevitably requiring a large number of free parameters in the fit. On the other, the initial dataset was sparse. The 358 levels characterised for the most abundant ^{58}NiH species span a relatively large energy region due to the large vibrational constant - the highest levels are about 8000 cm^{-1} above the origin. The experimental dataset was also unevenly distributed over the states and the vibrational numbers, with more than half the observations corresponding to the ground $^2\Delta$ state.

Hoping to retain physically reasonable shapes for the coupling spin-orbit functions, we compared them with Marian's *ab initio* results given in Ref [2]. These predict slow and small variation of $A_{\Pi\Pi}(R)$, $A_{\Delta\Delta}(R)$ and $\alpha_{\Pi\Delta}(R)$ with internuclear distance. But it quickly became clear that the theory-based R -dependence of the theoretical prediction for the $^2\Sigma^+ - ^2\Pi_{1/2}$ off-diagonal spin-orbit function $\alpha_{\Sigma\Pi}(R)$ could not reproduce the experimental observations. This coupling has significant impact on most eigenvalues. We therefore allowed the points defining $\alpha_{\Sigma\Pi}(R)$ below 2.25 \AA to become free parameters, and accepted its fitted form (see Fig. 5).

In addition to the SVD strategy, parameter correlation issues can be dealt with to some extent by careful choice of the number of fitted parameters. In order to find a ‘‘stable’’ pointwise representation of PECs for the three doublet states, the number of potential parameters was varied between 16 and 24. The final $^2\Sigma^+$ and $^2\Pi$ potentials are represented with 17 points, and the $^2\Delta$ potential with 18 points. The final coupling functions are defined by 3 – 5 points. Once the unweighted rms deviation of the fit approached 0.01 cm^{-1} , the shapes of the model functions were reviewed more carefully. Correlations can sometimes introduce wavy, unphysical shapes that be corrected by constraining some parameters to a reasonable form and refitting the remaining correlated parameters. The ‘‘reasonable’’ shape of a function, however, is not always well defined, so in some cases we used regularization (implemented as described by Eq.(7) in Ref [27]). The regularization procedure adds weighted squared deviations between selected model functions and their ‘‘reasonable’’ values to the merit function χ^2 . In this way the fitted functions are coaxed to stay as close as possible to these reasonable values without compromising the root mean square deviation of the final fit.

This fine-tuning of the model functions revealed that there was no need to specify separate $q_i(R)$ function for the e and the f symmetry, and that a single second-order function per state sufficed. All attempts to reduce the strong deviations of the $\beta(R)$ and the $\gamma(R)$ functions from the initially estimated value of unity were unsuccessful. The final shapes of the model functions are illustrated in the next section, and corresponding parameters are given in the supplementary material [38].

At this stage, we added the data for ^{60}NiH and ^{62}NiH to the fit. We expected that the mass dependence of the adiabatic correction to be negligible for when the heavy-atom substitution and this turned out to be the case - the data for all 3 isotopologues were reproduced within the estimated uncertainties without correction to the potential curves.

V. RESULTS OF THE FIT

A total of 753 levels belonging to the three Ni isotopes (358 from ^{58}NiH , 275 from ^{60}NiH , 120 from ^{62}NiH) were reproduced with an unweighted rms deviation of 0.014 cm^{-1} . Fig. 3 shows the ‘calculated - observed’ energy

residuals for the three NiH isotopologues computed from the optimized model functions. The calculated levels for each isotopologue and symmetry are referenced to the level $v = 0$ and $J = 2.5$ of the ground state (i.e. $T[{}^2\Delta, v=0, J=2.5, e \text{ and } f] = 0.0 \text{ cm}^{-1}$).

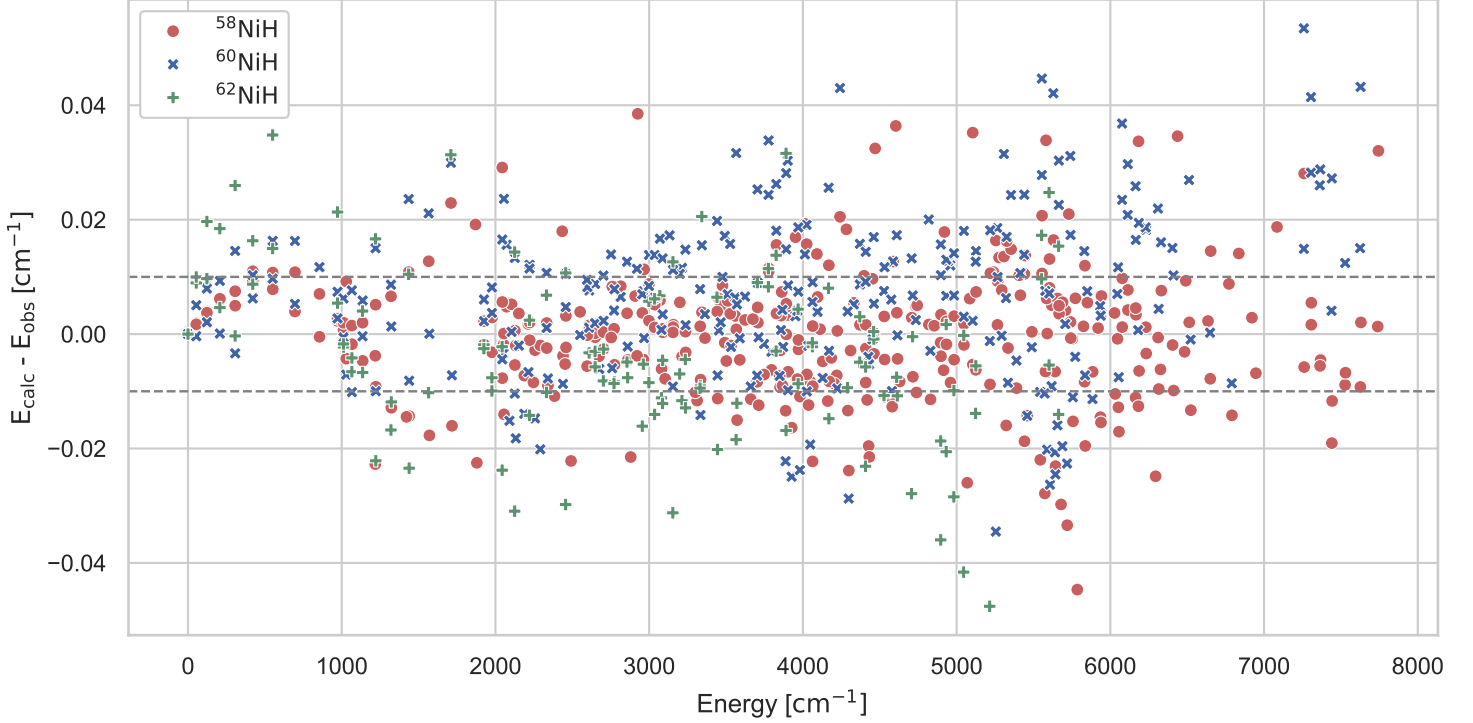


FIG. 3. Deviations of the term energies calculated with the deperturbed model functions described in this paper from the observed term energies for the three NiH isotopologues. The two dashed horizontal lines in the middle indicate the bounds of the estimated 1σ experimental uncertainty. The rms for ⁵⁸NiH data is 0.011 cm^{-1} , for ⁶⁰NiH data -0.015 cm^{-1} and for ⁶²NiH -0.015 cm^{-1} .

The final PECs parameters are listed in Table V.

In Fig. 4 the theoretical potential energy curves calculated in Ref [35] (circles) and the optimized potentials obtained in the present study (solid lines) for each electronic state are compared. Given the complexity of the system and the difficulties accompanying the theoretical calculations, the consistency between the slope and position of the inner and outer walls between both sets of curves is remarkable, even if at the potential minima the curves do not coincide. In the inset of the same figure the optimized potentials from this study are compared with the RKR potentials from Ref. [5]. One can see that the RKR curves (which were the starting potentials in our analysis) give more accurate results around R_e than the theoretical ones, but the slope of the outer wall differs significantly.

In Fig. 5 comparison between the diagonal and off-diagonal spin-orbit functions from our work with the theoretically calculated in Ref. [2] is shown. The overall agreement is very good, however some deviations are quite marked. The final results confirm the expectation that the diagonal SO functions are nearly independent of the internuclear distance. Unlike the almost constant value of the nondiagonal $\alpha_{\Pi\Delta}$ spin-orbit function, we have established that $\alpha_{\Sigma\Pi}$ spin-orbit function has somewhat stronger R -dependence towards smaller R values than predicted. The optimized $\alpha_{\Sigma\Pi}$ function resembles in general the behaviour of the theoretical curve, the absolute value of both functions decreases at smaller R , although the functional forms and the magnitude are not the same - the main difference being the more rapid and steep decrease of the theoretical curve.

On the left-hand side of Fig. 6 our final rotational $\beta(R)$ functions are shown and compared with the available *ab initio* functions from Ref. [2]. In the range where significant amount of experimental data is available their magnitudes and the dependence of the internuclear distance are reasonably close.

In the previous section it was discussed that a model incorporating only PECs, SO, LJ and LS R -dependent model functions and applied to the whole dataset is unable to give satisfactory results. To fit the data to experimental accuracy, the model had to be expanded by introducing (expected) corrections for spin-rotation coupling and additional

TABLE II. PECs parameters for the $^2\Delta$, $^2\Sigma^+$ and $^2\Pi$ states of ^{58}NiH . In order to interpolate in arbitrary intermediate point a natural cubic spline through all points in the interval from 0.75 Å to 3.0 Å should be applied.

R, Å	$U_{\Delta}(R)$, cm^{-1}	R, Å	$U_{\Pi}(R)$, cm^{-1}	$U_{\Sigma}(R)$, cm^{-1}
0.75000	57427.9282	0.75000	58327.9282	57827.9282
0.89062	35877.9282	0.89062	37027.9282	36327.9282
1.04347	18265.1273	0.99456	24743.8314	23867.2781
1.14130	9442.0370	1.11684	14759.6786	13829.2036
1.19021	6249.6905	1.21467	9173.8576	8151.8415
1.26358	2922.5813	1.28804	5767.9978	4928.7240
1.36141	602.4575	1.38586	3162.9113	2660.8467
1.45923	0.0000	1.50815	2227.0220	1928.2047
1.55706	519.5383	1.63043	2879.5323	2677.8026
1.66406	1885.1231	1.75271	4425.9655	4252.8068
1.77717	3838.0603	1.85054	6019.5544	5859.9990
1.87500	5733.7359	1.97282	8151.8841	7997.3996
1.97282	7682.6253	2.08593	10461.1010	10305.4060
2.07065	9617.2300	2.22656	13257.9981	13100.8780
2.22656	12752.1005	2.36718	15879.0454	15727.4369
2.41304	16190.9468	2.50781	17901.4169	17787.0570
2.65760	19318.7038	3.00000	22437.9282	22397.9282
3.00000	22342.9282	-	-	-

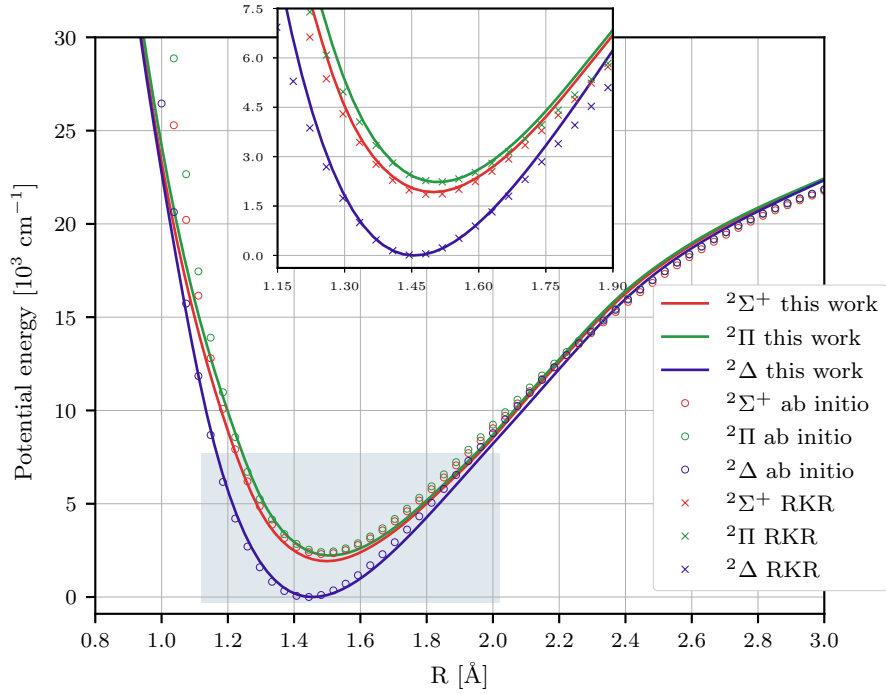


FIG. 4. Comparison between the theoretical potential energy curves calculated in Ref. [35] (circles) and the optimized potentials obtained in the present study (solid lines) for each electronic state. Inset: comparison between the constructed RKR potentials from Ref. [5] (crosses) and the optimized potentials obtained in the present study (solid lines). The darkened region from the bottom of the ground state up to 8000 cm^{-1} indicates the range of experimental energy terms.

Born-Oppenheimer breakdown effects. But improvement in the rms deviation came at the price of undesirable parameter correlation issues. Therefore we tried to retain the most plausible contributions in our fits. We discuss parameter correlation and give a correlation matrix in Appendix A, which is part of the Supplementary Material [38].

Pure spin-rotation effects are expected to be small, but we recall that second-order interactions which include both the spin-orbit and L-uncoupling operators [39] lead to the same functional effect as the spin-rotation operator (see,

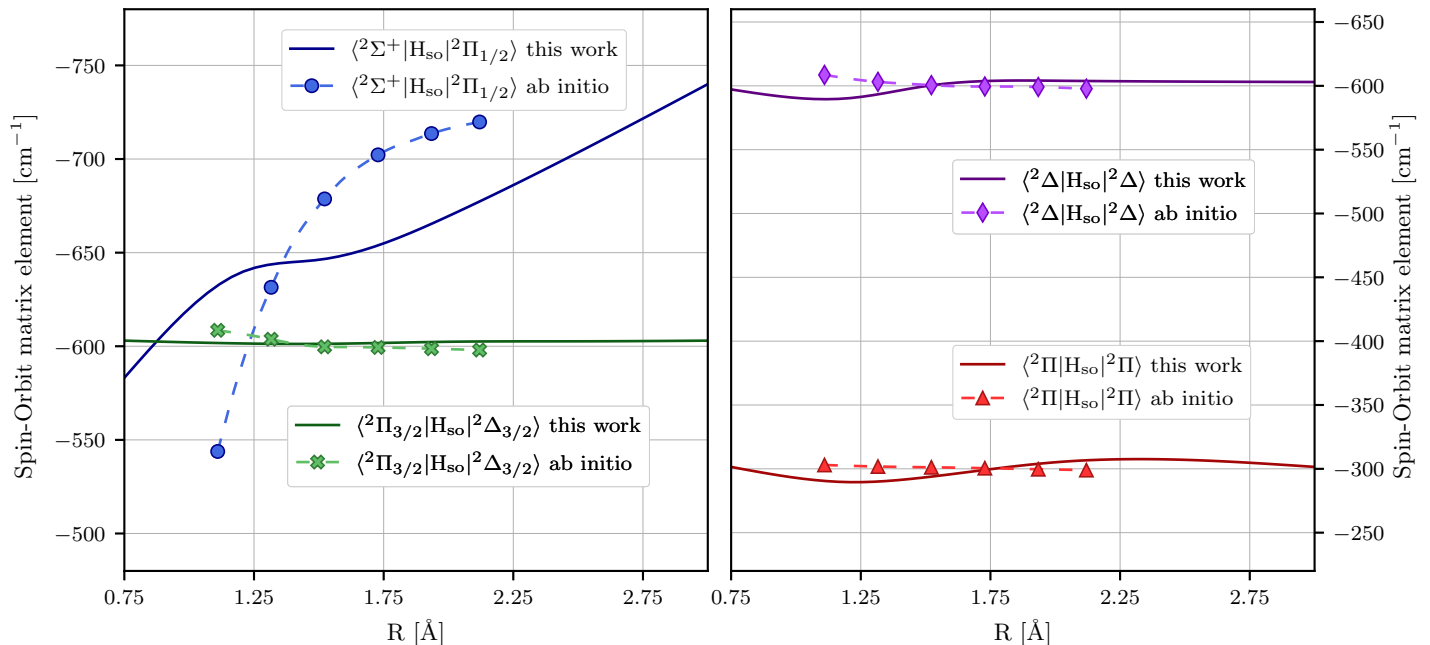


FIG. 5. Comparison of the spin-orbit matrix elements obtained in the present work (solid lines) with the theoretically calculated (dashed lines) ones by C. Marian in Ref. [2]. On the left-hand side the off-diagonal spin-orbit matrix elements are compared. The matrix elements $\langle {}^2\Pi_{1/2} | H_{\text{so}} | {}^2\Sigma_{1/2}^+ \rangle$ and $\langle {}^2\Delta_{3/2} | H_{\text{so}} | {}^2\Pi_{3/2} \rangle$ are determined through the functions $\alpha_{\Sigma\Pi}(R)$ and $\alpha_{\Pi\Delta}(R)$ respectively according to Eq. (14) and Eq. (15). On the right-hand side the diagonal spin-orbit matrix elements are compared. The matrix elements $\langle {}^2\Pi_{\Omega} | H_{\text{so}} | {}^2\Pi_{\Omega} \rangle$ and $\langle {}^2\Delta_{\Omega} | H_{\text{so}} | {}^2\Delta_{\Omega} \rangle$ are determined through the functions $A_{\Pi\Pi}(R)$ and $A_{\Delta\Delta}(R)$ respectively according to Eq. (12) and Eq. (13).

for example, the discussion in [50]). The rotational $\gamma(R)$ functions are shown on the right-hand side of Fig. 6. If this effective spin-rotation interaction could be ignored, the γ functions would be constant and equal to unity. The model has shown that this is nearly true for the $\gamma_{\Sigma\Sigma}$ function, but that $\gamma_{\Pi\Pi}$ and $\gamma_{\Delta\Delta}$ change significantly with internuclear distance.

We believe that within the system of the coupled lower states in NiH the model is complete, but we were forced to introduce the second order $f_i(R)$ corrections. They are modeled through the $q_i(R)$ functions shown in Fig. 7. The fit was clearly less successful without them. They allow to account for possible J -dependent interactions with remote electronic states through the \mathbf{H}_{rot} operator.

VI. DISCUSSION AND CONCLUSIONS

This description of the three lowest electronic states in NiH is the first to reach experimental uncertainties in the residuals of a term energy fit for this radical by direct solution of system of coupled Schrödinger equations. The model evolved to has effectively identified shortcomings in the atomic-parameter based - and instinctively meaningful “supermultiplet” approach that has so far been envisaged to describe the three electronic states of NiH dissociating to the lowest Ni + H atomic asymptote. The most important of these is a variation of spin-orbit state-mixing effects as a function of internuclear distance. By optimising radial functions over the restricted range of R accessible from spectroscopic data, and retaining *ab initio* predictions elsewhere, we believe that the current potential-curve and coupling functions may be extrapolated to higher rotational states than are actually observed. The predictive power of the model has already been assessed when assigning the reported new spectroscopic observations (Table 1) in ${}^2\Sigma_{1/2}^+$ and ${}^2\Pi_{1/2}$ states. The model is able to provide the current best predictions for infrared transitions (rovibrational transitions within a given state, as well as rovibronic transitions between members of the supermultiplet states), susceptible to be seen for example in stellar atmospheres. We supply this information as supplementary material, as a step towards providing information for data bases such as MoLList [10] or ExoMol. The entry for NiH in the 2020 release of ExoMol [11] noted specifically the lack of input for NiH. This work can provide transition wavenumbers with confidence, but not absorption cross-sections, for which transition dipole moment functions would also be required.

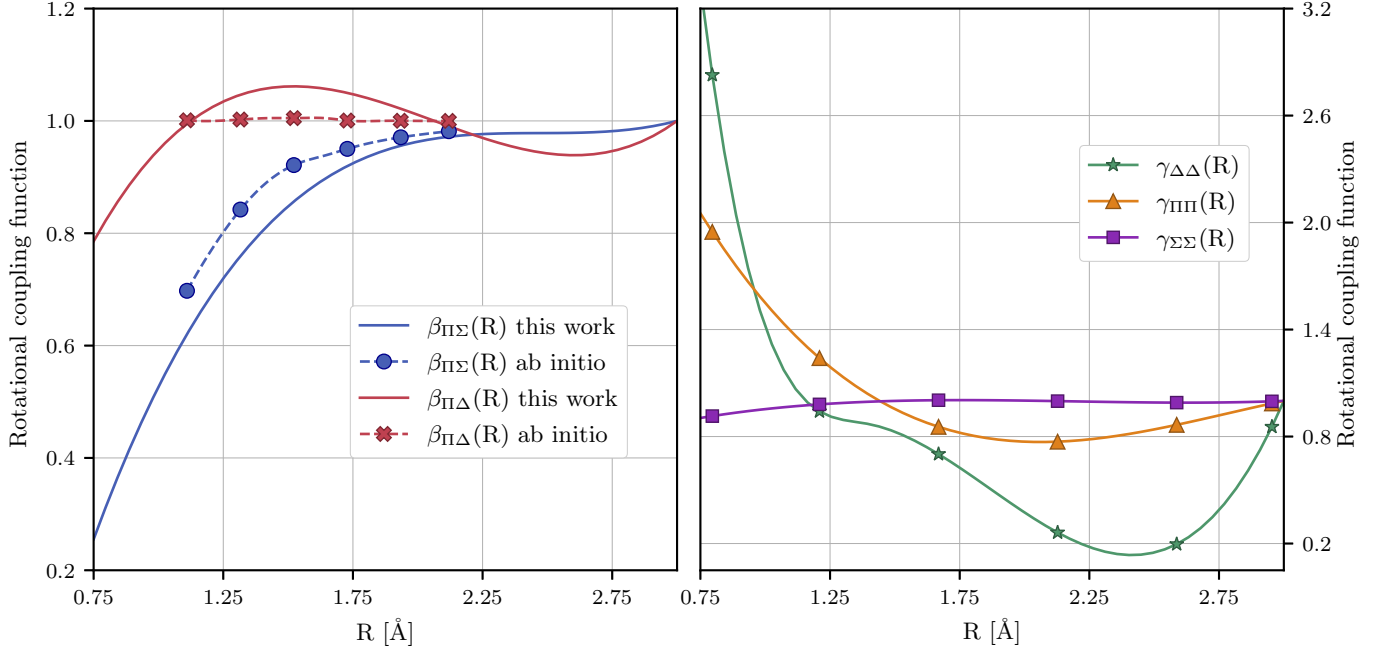


FIG. 6. The rotational coupling functions calculated in the present work. On the left-hand side: the calculated rotational $\beta(R)$ coupling functions (solid lines, see section III B) are compared with the *ab initio* values from Ref. [2] (dashed lines). Note that the theoretical matrix element between ${}^2\Sigma^+$ and ${}^2\Pi$ states is divided by a factor of $\sqrt{L(L+1)}/\sqrt{2}$. On the right-hand side: the fitted rotational $\gamma(R)$ functions (see section III D) due to the spin-rotation and second-order interactions.

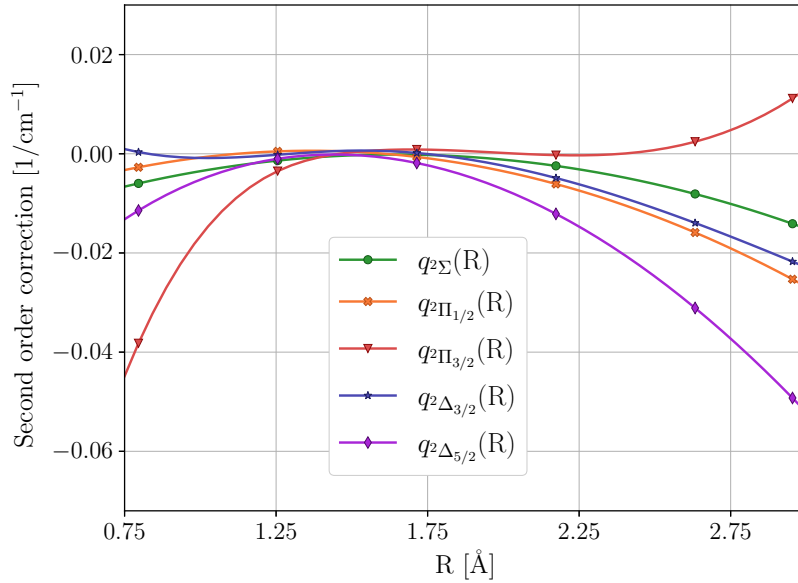


FIG. 7. Second-order correction functions. See section III E for details.

It can be however anticipated that the branch intensities will be affected by spin-orbit mixing, and relative intensities could be predicted taking this into account. Lipus *et al* [8] likewise discussed this. They measured spin-changing transitions within the ${}^2\Delta$ state, and claimed that although these are electric-dipole forbidden in Hund's case (a), they acquired some electric-dipole transition moment through rotational couplings, and that this electric dipole contribution to intensities was greater than (allowed) magnetic dipole contributions.

The shapes of the model functions should be considered with caution. The complexity of the model, the number

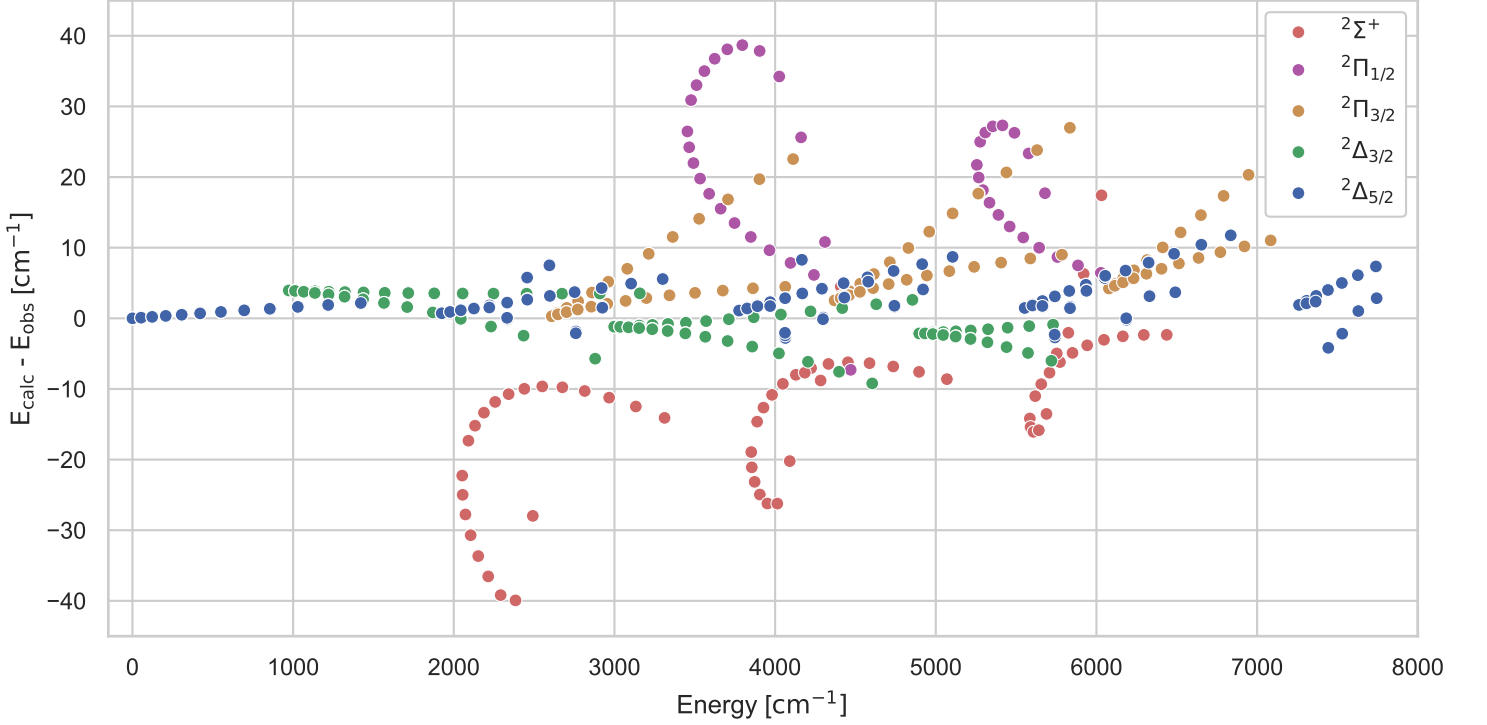


FIG. 8. Residuals of the energies for ^{58}NiH calculated with the optimized potential functions but with the initial and expected values for the coupling functions $\beta(R) = 1$, $\gamma(R) = 1$, $q(R) = 0$; $A(R)$ and $\alpha(R)$ are the theoretical functions taken from [2].

of parameters and the sparse structure of the data set lead to strong correlations between the fitted parameters. We observed that similar fit quality can be achieved with different model functions. Most of them could be rejected due to their unphysical appearance, but since it is a question of subjective judgement, it is very difficult to appreciate the true uncertainty of the fitted model functions and thus the predictive power of the model. The best we can do was to try to keep the model functions as close to the theoretical predictions as possible. We are confident that the deviations between the fitted functions and the theoretical expectation (see Fig. 5 and Fig. 6) are significant. To demonstrate this in Fig. 8 we present the residuals for ^{58}NiH computed with the fitted potentials, but with the coupling functions fixed to the theoretical expectations (all $\beta(R) = 1$ and $\gamma(R) = 1$, all $q(R) = 0$ and $A(R)$ and $\alpha(R)$ as in [2]). Apparently the model is very sensitive to the shape of these functions and even though the calculated functions are of the same order of magnitude as the fitted ones, they are not able to reproduce experimental data even qualitatively. Nevertheless without theoretical predictions, it would be much more difficult to provide decent starting values of the model functions and then to eliminate unsuitable solutions. Experimental spectroscopy and high quality theoretical predictions clearly go hand in hand.

Having achieved a successful treatment of NiH data, one would expect the experimental data in ^{58}NiD should be reproduced correctly by the model. When the same coupled-channels model (Figure 2) is applied independently to ^{58}NiD , an rms deviation of residuals close to the experimental uncertainty can indeed be achieved. A combined analysis of both NiH and NiD, however, would need an extension of the model with separate Born-Oppenheimer breakdown functions for substitution of Ni and H isotopes (as e.g. in [42]). First attempts to do this showed us that it is a problem which requires to start the fitting procedure nearly from the beginning and face again the problems of ambiguity and strong correlations between the model functions. In addition, at present data are available for ^{58}NiD only. Future work will aim to extend the dataset to include ^{60}NiD and possibly ^{62}NiD , before attempting the multi-isotope coupled-channel treatment of NiH and NiD together.

ACKNOWLEDGMENTS

Authors acknowledge partial support from the Bulgarian National Science Fund through Grant D18/12/2017. I.H. acknowledges partial support by the National program - Young scientists and postdoctoral candidates 2020 of Ministry of Education and Science and Project 80.09-72/2019 of the Sofia University.

Author contributions: IH: software, methodology, spectral analysis, writing - original draft preparation, writing - review and editing; IB: analysis of raw spectra; AJR: experiment and data collection, spectral analysis, writing - review and editing; PC: experiment and data collection, writing - review and editing; AP: conceptualization, methodology, supervision, spectral analysis, writing - review and editing, funding acquisition.

-
- [1] Jeffrey A. Gray, Mingguang Li, Thomas Nelis, and Robert W. Field. The electronic structure of NiH: the $\text{Ni}^+ 3d^9 2D$ supermultiplet. *The Journal of Chemical Physics*, 95(10):7164–7178, Nov 1991.
 - [2] C. M. Marian. Quasirelativistic calculation of the vibronic spectra of NiH and NiD. *The Journal of Chemical Physics*, 93(2):1176–1186, Jul 1990.
 - [3] Christel M. Marian, Margareta R. A. Blomberg, and Per E. M. Siegbahn. Multireference and relativistic effects in NiH. *The Journal of Chemical Physics*, 91(6):3589–3595, Sep 1989.
 - [4] Amanda J. Ross, Patrick Crozet, Cyril Richard, Heather Harker, Stephen H. Ashworth, and Dennis W. Tokaryk. Resolved fluorescence spectra of NiH. Electronic structure, electronic energy transfer, and the Zeeman effect in low-lying states. *Molecular Physics*, 110(17):2019–2033, Sep 2012.
 - [5] Mahdi Abbasi, Alireza Shayesteh, Patrick Crozet, and Amanda J. Ross. Observation of low-lying electronic states of NiD with multi-isotope analysis. *Journal of Molecular Spectroscopy*, 349:49–59, Jul 2018.
 - [6] Raphaël Vallon, Cyril Richard, Patrick Crozet, Ghassan Wannous, and Amanda Ross. Laboratory Measurements of NiH by Fourier Transform Dispersed Fluorescence. *Astrophysical Journal*, 696(1):172–175, Apr 2009.
 - [7] K. Lipus, U. Simon, E. Bachem, Th. Nelis, and W. Urban. Direct observation of the fundamental vibration-rotation transitions within the NiD $X^2\Delta_{5/2}$ ground state by CO-Faraday-L.M.R. spectroscopy and zero field transitions in NiH. *Molecular Physics*, 67(6):1431–1437, Aug 1989.
 - [8] K. Lipus, E. Bachem, and W. Urban. Direct observation of fine structure transitions within the $X^2\Delta$ ground-state of the NiH radical by CO₂-Faraday laser magnetic-resonance. *Molecular Physics*, 75(4):945–951, Mar 1992.
 - [9] Timothy C. Steimle, David F. Nachman, Jeffrey E. Shirley, David A. Fletcher, and John M. Brown. The microwave spectrum of NiH. *Molecular Physics*, 69(5):923–932, Apr 1990.
 - [10] P. Bernath. Mollist: Molecular line lists, intensities and spectra. *Journal of Quantitative Spectroscopy and Radiative Transfer*, 240:46–64, 2020.
 - [11] Jonathan Tennyson, Sergei N. Yurchenko, Ahmed F. Al-Refaeie, Victoria H.J. Clark, Katy L. Chubb, Eamon K. Conway, Akhil Dewan, Maire N. Gorman, Christian Hill, A.E. Lynas-Gray, Thomas Mellor, Laura K. McKemmish, Alec Owens, Oleg L. Polyansky, Mikhail Semenov, Wilfrid Somogyi, Giovanna Tinetti, Apoorva Upadhyay, Ingo Waldmann, Yixin Wang, Samuel Wright, and Olga P. Yurchenko. The 2020 release of the exomol database: Molecular line lists for exoplanet and other hot atmospheres. *Journal of Quantitative Spectroscopy and Radiative Transfer*, 255:107228, 2020.
 - [12] Jonathan Tennyson, Lorenzo Lodi, Laura K. McKemmish, and Sergei N. Yurchenko. The ab initio calculation of spectra of open shell diatomic molecules. *Journal of Physics B: At. Mol. Opt. Phys.*, 49(10):102001, May 2016.
 - [13] Heng Ying Li, Jonathan Tennyson, and Sergei N Yurchenko. ExoMol line lists – XXXII. The rovibronic spectrum of MgO. *Monthly Notices of the Royal Astronomical Society*, 486(2):2351–2365, Apr 2019.
 - [14] Laura K. McKemmish, Thomas Masseron, H. Jens Hoeijmakers, Víctor Pérez-Mesa, Simon L. Grimm, Sergei N. Yurchenko, and Jonathan Tennyson. ExoMol molecular line lists – XXXIII. The spectrum of Titanium Oxide. *Monthly Notices of the Royal Astronomical Society*, 488(2):2836–2854, 07 2019.
 - [15] Warren M. Kosman and Juergen Hinze. Inverse perturbation analysis: Improving the accuracy of potential energy curves. *Journal of Molecular Spectroscopy*, 56(1):93–103, Apr 1975.
 - [16] C.R. Vidal and H. Scheingraber. Determination of diatomic molecular constants using an inverted perturbation approach. *Journal of Molecular Spectroscopy*, 65(1):46–64, Apr 1977.
 - [17] John A. Coxon and Photos G. Hajigeorgiou. Isotopic dependence of Born-Oppenheimer breakdown effects in diatomic hydrides: The $B^1\Sigma^+$ and $X^1\Sigma^+$ states of HF and DF. *Journal of Molecular Spectroscopy*, 142(2):254–278, Aug 1990.
 - [18] John A. Coxon and Photos G. Hajigeorgiou. Isotopic dependence of Born-Oppenheimer breakdown effects in diatomic hydrides: The $B^1\Sigma^+$ and $X^1\Sigma^+$ states of HCl and DCl. *Journal of Molecular Spectroscopy*, 139(1):84–106, Jan 1990.
 - [19] H. Martin. Empirically fitting the potential energy curves for the X, B, and B' double minimum and the $D^2\Sigma^+$ states in CaH using united knowledge of CaH and CaD. *The Journal of Chemical Physics*, 88(3):1797–1806, Feb 1988.
 - [20] Christina Carlsund-Levin, Nils Elander, Alonso Nunez, and Armin Scrinzi. An exterior complex rotated coupled channel description of predissociation in diatomic molecules applied to a model of the four lowest $^2\Sigma^+$ states in CaH. *Physica Scripta*, 65(4):306–322, Jan 2002.
 - [21] Kyohei Watanabe, Iori Tani, Kaori Kobayashi, Yoshiki Moriwaki, and Stephen C. Ross. Laser spectroscopic study of the

- B/ $B^2\Sigma^+ - X^2\Sigma^+$ (9-0), (10-0), (11-0) and (18-0) bands of CaH. *Chemical Physics Letters*, 710:11–15, Oct 2018.
- [22] W. Jastrzębski, P. Kowalczyk, and A. Pashov. The perturbation of the $B^1\Pi$ and $C^1\Sigma^+$ states of KLi. *Journal of Molecular Spectroscopy*, 209:50–56, 2001.
- [23] Milena Ivanova, Alexander Stein, Asen Pashov, Horst Knöckel, and Eberhard Tiemann. The $B^1\Pi$ and $C^1\Sigma^+$ states of LiRb. *The Journal of Chemical Physics*, 138(9):094315, Mar 2013.
- [24] I. Havalyova, A. Pashov, P. Kowalczyk, J. Szczepkowski, and W. Jastrzębski. The coupled system of $(5)^1\Sigma_u^+$ and $(5)^1\Pi_u$ electronic states in Rb_2 . *Journal of Quantitative Spectroscopy and Radiative Transfer*, 202:328–334, Nov 2017.
- [25] Horst Knöckel, Steffen Rühmann, and Eberhard Tiemann. The $A^1\Sigma_u^+$ system of Mg_2^+ . *Eur. Phys. J. D*, 68(10), Oct 2014.
- [26] Heather Harker, Patrick Crozet, Amanda J. Ross, Kara Richter, Joshua Jones, Carl Faust, John Huennekens, Andrey V. Stolyarov, Houssam Salami, and Thomas Bergeman. Experimental and theoretical studies of the coupled $A^1\Sigma^+$ and $b^3\Pi$ states of NaK. *Physical Review A*, 92(1), Jul 2015.
- [27] K. Alps, A. Kruzins, M. Tamanis, R. Ferber, E. A. Pazyuk, and A. V. Stolyarov. Fourier-transform spectroscopy and deperturbation analysis of the spin-orbit coupled $A^1\Sigma^+$ and $b^3\Pi$ states of KRb. *The Journal of Chemical Physics*, 144(14):144310, Apr 2016.
- [28] A. N. Drozdova, A. V. Stolyarov, M. Tamanis, R. Ferber, P. Crozet, and A. J. Ross. Fourier transform spectroscopy and extended deperturbation treatment of the spin-orbit coupled $A^1\Sigma_u^+$ and $b^3\Pi_u$ states of the Rb_2 molecule. *Physical Review A*, 88(2), Aug 2013.
- [29] Jianmei Bai, E. H. Ahmed, B. Beser, Y. Guan, S. Kotochigova, A. M. Lyra, S. Ashman, C. M. Wolfe, J. Huennekens, Feng Xie, Dan Li, Li Li, M. Tamanis, R. Ferber, A. Drozdova, E. Pazyuk, A. V. Stolyarov, J. G. Danzl, H.-C. Nägerl, N. Bouloufa, O. Dulieu, C. Amiot, H. Salami, and T. Bergeman. Global analysis of data on the spin-orbit-coupled $A^1\Sigma_u^+$ and $b^3\Pi_u$ states of Cs_2 . *Physical Review A*, 83(3), Mar 2011.
- [30] A. Pashov, P. Kowalczyk, A. Grochola, J. Szczepkowski, and W. Jastrzębski. Coupled-channels analysis of the $(5)^1\Sigma_u^+$, $5^1\Pi_u$, $5^3\Pi_u$, $2^3\Delta_u$ complex of electronic states in rubidium dimer. *Journal of Quantitative Spectroscopy and Radiative Transfer*, 221:225–232, Dec 2018.
- [31] J. Szczepkowski, A. Grochola, P. Kowalczyk, W. Jastrzębski, E.A. Pazyuk, A.V. Stolyarov, and A. Pashov. The spin-orbit coupling of the $6^1\Sigma^+$ and $4^3\Pi$ states in KCs: Observation and deperturbation. *Journal of Quantitative Spectroscopy and Radiative Transfer*, 239:106650, Dec 2019.
- [32] Satyender Goel and Artëm E. Masunov. Potential energy curves and electronic structure of 3d transition metal hydrides and their cations. *The Journal of Chemical Physics*, 129(21):214302, Dec 2008.
- [33] Vincenzo Barone and Carlo Adamo. First-row transition-metal hydrides: A challenging playground for new theoretical approaches. *International Journal of Quantum Chemistry*, 61(3):443–451, 1997.
- [34] James Shee, Benjamin Rudshiteyn, Evan J. Arthur, Shiwei Zhang, David R. Reichman, and Richard A. Friesner. On achieving high accuracy in quantum chemical calculations of 3d transition metal-containing systems: A comparison of auxiliary-field quantum monte carlo with coupled cluster, density functional theory, and experiment for diatomic molecules. *Journal of Chemical Theory and Computation*, 15(4):2346–2358, Mar 2019.
- [35] Wenli Zou and Wenjian Liu. Theoretical study on the low-lying electronic states of NiH and NiAt. *J. Comput. Chem.*, 28(14):2286–2298, 2007.
- [36] R. Vallon, S.H. Ashworth, P. Crozet, R.W. Field, D. Forthomme, H. Harker, C. Richard, and A.J. Ross. A room-temperature metal-hydride discharge source, with observations on NiH and FeH. *Journal of Physical Chemistry A*, 113(47):13159, 2009.
- [37] A. Kramida, Y. Ralchanko, J. Reader, and NIST ASD Team. NIST Atomic Spectra Database (ver. 5.7.1), [online]. Available: <http://physics.nist.gov/asd>, 2019. National Institute of Standards and Technology, Gaithersburg, MD.
- [38] Supplementary material, containing experimental data and the fitted parameters of the model.
- [39] Helene Lefebvre-Brion and Robert Field. *The Spectra and Dynamics of Diatomic Molecules*. Academic Press, 2004.
- [40] Christian G. Parigger and James O. Hornkohl. Diatomic molecular spectroscopy with standard and anomalous commutators. *International Review of Atomic and Molecular Physics*, 1:25, 2010.
- [41] P.R. Bunker and R.E. Moss. The breakdown of the Born-Oppenheimer approximation: the effective vibration-rotation Hamiltonian for a diatomic molecule. *Molecular Physics*, 33(2):417–424, Feb 1977.
- [42] Robert J. Le Roy. Improved parameterization for combined isotopomer analysis of diatomic spectra and its application to HF and DF. *Journal of Molecular Spectroscopy*, 194(2):189–196, Apr 1999.
- [43] Ronnie Kosloff. Time-dependent quantum-mechanical methods for molecular dynamics. *Journal of Physical Chemistry*, 92(8):2087–2100, Apr 1988.
- [44] C. Clay Marston and Gabriel G. Balint-Kurti. The Fourier grid Hamiltonian method for bound state eigenvalues and eigenfunctions. *The Journal of Chemical Physics*, 91(6):3571–3576, Sep 1989.
- [45] James K.G. Watson. Robust weighting in least-squares fits. *Journal of Molecular Spectroscopy*, 219(2):326–328, Jun 2003.
- [46] W. H. Press, S. A. Teukolsky, W. T. Vetterling, and B. P. Flannery. *Numerical Recipes in C: The Art of Scientific Computing*. Cambridge University Press, 1992.
- [47] Pauli Virtanen, , Ralf Gommers, Travis E. Oliphant, Matt Haberland, Tyler Reddy, David Cournapeau, Evgeni Burovski, Pearu Peterson, Warren Weckesser, Jonathan Bright, Stéfan J. van der Walt, Matthew Brett, Joshua Wilson, K. Jarrod Millman, Nikolay Mayorov, Andrew R. J. Nelson, Eric Jones, Robert Kern, Eric Larson, C J Carey, İlhan Polat, Yu Feng, Eric W. Moore, Jake VanderPlas, Denis Laxalde, Josef Perktold, Robert Cimrman, Ian Henriksen, E. A. Quintero, Charles R. Harris, Anne M. Archibald, Antônio H. Ribeiro, Fabian Pedregosa, and Paul van Mulbregt. SciPy 1.0: fundamental algorithms for scientific computing in Python. *Nature Methods*, 17(3):261–272, Feb 2020.
- [48] A. Pashov, W. Jastrzębski, and P. Kowalczyk. Construction of potential curves for diatomic molecular states by the IPA

- method. *Computer Physics Communications*, 128(3):622–634, Jun 2000.
- [49] I. Havalayova and A. Pashov. An open-source Python library for calculating energy levels and spectra of diatomic molecules. <https://github.com/ihavalayova/diatomic>, 2021.
- [50] Milena Ivanova, Alexander Stein, Asen Pashov, Andrey V. Stolyarov, Horst Knöckel, and Eberhard Tiemann. The $X^2\Sigma^+$ state of LiCa studied by Fourier-transform spectroscopy. *The Journal of Chemical Physics*, 135(17):174303, Nov 2011.